Critical Role of Polymer Aggregation and Miscibility in Nonfullerene-Based Organic Photovoltaics

Xueping Yi, Zhengxing Peng, Bing Xu, Dovletgeldi Seyitliyev, Carr Hoi Yi Ho, Evgeny O. Danilov, Taesoo Kim, John R. Reynolds, Aram Amassian, Kenan Gundogdu, Harald Ade, and Franky So*

Understanding the correlation between polymer aggregation, miscibility, and device performance is important to establish a set of chemistry design rules for donor polymers with nonfullerene acceptors (NFAs). Employing a donor polymer with strong temperature-dependent aggregation, namely PffBT4T-2OD [poly[(5,6-difluoro-2,1,3-benzothiadiazol-4,7-diyl)-*alt*-(3,3‴-di(2-octyldodecyl)-2,2′;5′,2″;5″,2‴-quaterthiophen-5,5-diyl)], also known as PCE-11 as a base polymer, five copolymer derivatives having a different thiophene linker composition are blended with the common NFA O-IDTBR to investigate their photovoltaic performance. While the donor polymers have similar optoelectronic properties, it is found that the device power conversion efficiency changes drastically from 1.8% to 8.7% as a function of thiophene content in the donor polymer. Results of structural characterization show that polymer aggregation and miscibility with O-IDTBR are a strong function of the chemical composition, leading to different donor–acceptor blend morphology. Polymers having a strong tendency to aggregate are found to undergo fast aggregation prior to liquid–liquid phase separation and have a higher miscibility with NFA. These properties result in smaller mixed donor–acceptor domains, stronger PL quenching, and more efficient exciton dissociation in the resulting cells. This work indicates the importance of both polymer aggregation and donor–acceptor interaction on the formation of bulk heterojunctions in polymer:NFA blends.

1. Introduction

With the recent progress made in nonfullerene acceptor (NFA)-based organic solar cells (OSCs) having a PCE exceeding 17%,[1] tremendous efforts have been dedicated to the development of new nonfullerene acceptors, which yield more efficient, more stable, and less-expensive photovoltaic materials than conventional fullerene acceptors.[2–5] Most recent advances in device performance have come from the development of NFAs. Compared to NFAs, the development of donor polymers has lagged behind owing to a lack of understanding of the chemistry design rules.

The photoactive layer of organic solar cells (OSCs) is a bulk heterojunction (BHJ) consisting of a blend of an electron donating polymer and electron accepting molecules finely mixed at the nanoscale.[6–8] An optimum morphology of the BHJ requires maximized donor/acceptor (D/A) interfaces for efficient exciton dissociation and a bicontinuous interpenetrating network for better charge extraction. Hence, controlling the BHJ morphology is a key to develop efficient organic solar cells. One of the most successful strategies for improving the device performance is by controlling the polymer aggregation, which is one of the critical factors determining the morphology of a polymer blend.[9–11]

However, due to the lack of an in-depth understanding of the requirements for polymer aggregation for optimum blend morphology, conflicting results have been reported. While some reports suggest that strong polymer aggregation is preferred to increase charge extraction efficiency, suppress bimolecular

X. Yi, Dr. C. H. Y. Ho, Dr. T. Kim, Prof. A. Amassian, Prof. F. So
Organic and Carbon Electronics Lab (ORaCEL)
Department of Materials Science and Engineering
North Carolina State University
Raleigh, NC 27695, USA
E-mail: fso@ncsu.edu
Z. Peng, D. Seyitliyev, Prof. K. Gundogdu, Prof. H. Ade
Department of Physics
Organic and Carbon Electronics Lab (ORaCEL)
North Carolina State University
Raleigh, NC 27695, USA

Dr. B. Xu, Prof. J. R. Reynolds
School of Chemistry and Biochemistry
School of Materials Science and Engineering
Center for Organic Photonics and Electronics
Georgia Tech Polymer Network
Georgia Institute of Technology
Atlanta, GA 30332, USA

Dr. E. O. Danilov
Department of Chemistry
North Carolina State University
Raleigh, NC 27695, USA

**ADVANCED
SCIENCE NEWS**
www.advancedsciencenews.com

**ADVANCED
ENERGY
MATERIALS**
www.advenergymat.de

recombination, and reduce the energy loss,[11–13] other works claim the strong aggregation of the polymer backbone leads to poor active layer morphology with excessively large domain sizes, which lower the device performance.[14–17] These inconsistencies indicate polymer aggregation is necessary, but not sufficient, for high performance OPVs. In addition to polymer aggregation, the morphology of the donor–acceptor (D-A) blend is also governed by the molecular interaction and miscibility between the polymer donor and the small molecule acceptor as well as the kinetics of phase separation during film formation.[18–20] Favorable donor–acceptor miscibility helps phase separation occur at appropriate length-scales during de-mixing of the blend component as the solvent evaporates.[21,22] Compared to fullerene molecules, the NFAs have shown many different physicochemical properties, such as high miscibility with donor polymers due to similar surface energy[23,24] and strong π–π interactions formed by electron-deficient end-capping units.[25] Thus, the development of new donor polymers matching the properties of NFAs requires a new understanding of the formation of the polymer-NFA photoactive blend.

In this work, we present a comprehensive study to uncover the polymer-aggregation-dependent device performance through an in-depth study by using five donor polymers, namely PffBT4T-2OD (T4T), PffBT3T-2OD (T3T), and three of their random terpolymers (PffBT4T$_{90}$-co-3T$_{10}$, PffBT4T$_{70}$-co-3T$_{30}$, and PffBT4T$_{50}$-co-3T$_{50}$) synthesized by varying the ratio between bithiophene to single thiophene linkers in the polymer backbone. We found that, despite the similarities in their molecular structure, these polymers display quite different temperature-dependent-aggregation (TDA) properties and show a large variation of PCE values from 1.8% for PffBT3T-2OD up to 8.7% for PffBT4T$_{90}$-co-3T$_{10}$ when blended with O-IDTBR ((5Z,5′Z)-

5,5′-(((4,4,9,9-tetraoctyl-4,9-dihydro-s-indaceno[1,2-b:5,6-b′]dithiophene-2,7-diyl)bis(benzo[c][1,2,5]thiadiazole-7,4-diyl))bis(methanylylidene))bis(3-ethyl-2-thioxothiazolidin-4-one)). In contrast, all three terpolymers were previously shown to yield high efficiencies when blended with fullerene (PCE > 9% for all terpolymer blends),[26] again demonstrating the fact that polymers designed for fullerenes do not necessarily work with NFAs. Specifically, we found that, in terms of interface exciton dissociation and bulk charge transport, the NFA-based device performance is strongly dependent on the aggregation properties of the donor polymers and their miscibility with the NFA. Results from in situ ultraviolet–visible (UV–vis) absorption, Resonant Soft X-ray Scattering (R-SoXS) and Differential Scanning Calorimetry (DSC) showed that the strongly aggregated polymers (PffBT4T-2OD and PffBT4T$_{90}$-co-3T$_{10}$) undergo fast polymer aggregation first in the polymer:IDTBR solution during spin-coating and have a high degree of miscibility with IDTBR to suppress liquid–liquid phase separation, forming well-mixed and multiscale domains. Due to the small mixed donor–acceptor domains in PffBT4T-2OD and PffBT4T$_{90}$-co-3T$_{10}$ devices, PL quenching is stronger and interfacial charge transfer is faster, signifying more efficient exciton dissociation and charge generation. In addition to O-IDTBR, we found that a similar polymer-aggregation-dependence is also observed in blends with another NFA—ITIC-M, demonstrating the universality of this finding.

2. Results and Discussion

Polymers PffBT4T-2OD, PffBT4T$_{90}$-co-3T$_{10}$, PffBT4T$_{70}$-co-3T$_{30}$, PffBT4T$_{50}$-co-3T$_{50}$, and PffBT3T-2OD having the repeat unit structures given in **Figure 1**a were synthesized by varying the
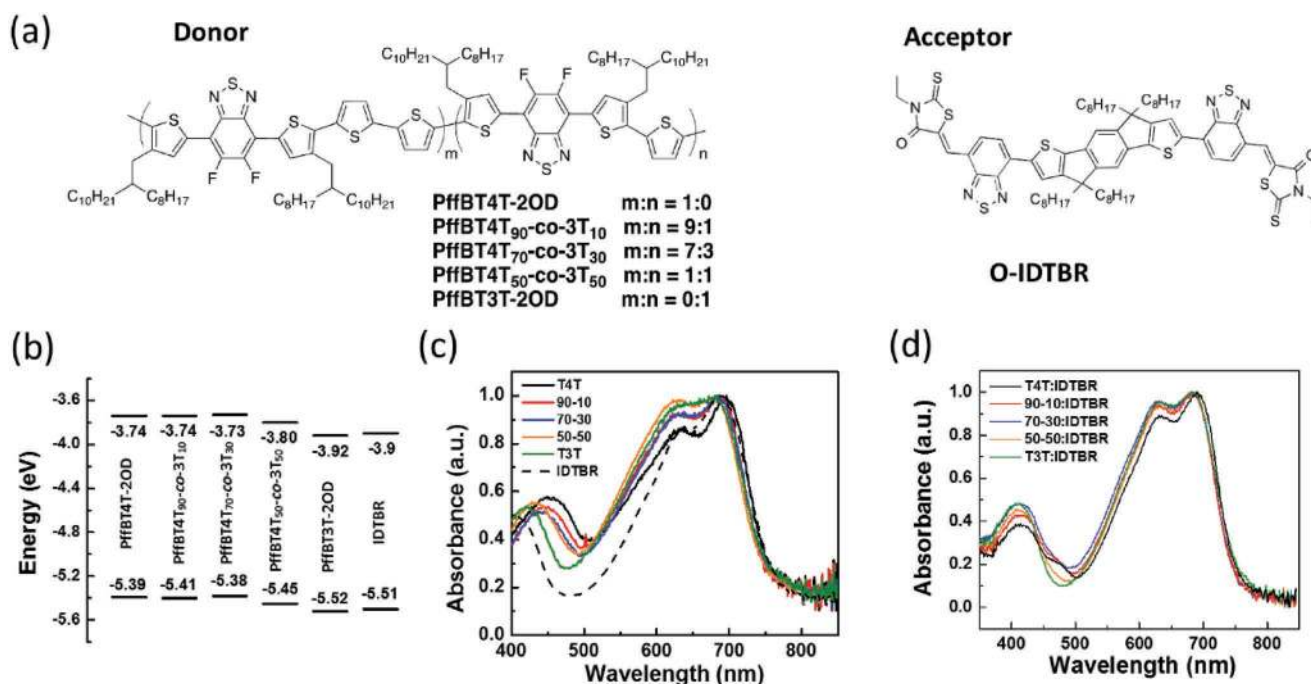

Figure 1. a) The chemical structures of PffBT4T-2OD, PffBT4T$_{90}$-co-3T$_{10}$, PffBT4T$_{70}$-co-3T$_{30}$, PffBT4T$_{50}$-co-3T$_{50}$, PffBT3T-2OD, and IDTBR; b) energy levels of the donor polymers determined by DPV (details are shown in our previous paper[26]); c) normalized absorbance spectra of pristine polymers and pristine IDTBR; d) normalized absorbance of polymer:IDTBR blend films.

ADVANCED
SCIENCE NEWS
www.advancedsciencenews.com

ADVANCED
ENERGY
MATERIALS
www.advenergymat.de

number of bithiophene to thiophene linkers in PffBT4T-2OD. We will refer to the PffBT4T-2OD homopolymer as T4T and the PffBT3T-2OD homopolymer as T3T throughout this work. The detailed synthesis approach and polymer structure verification can be found in our previous work.[26] As shown in Figure 1a, both T4T and T3T have the same acceptor moiety difluorobenzothiadiazole, surrounded by two flanking thiophene rings. On the other hand, the donor moieties for these polymers are different; T4T, containing bithiophene linkers, is known for its strong temperature-dependent aggregation (TDA) property that is clearly demonstrated by temperature-dependent UV–vis absorption.[3] As shown in Figure S1 (Supporting Information), the optical absorption spectrum for a T4T solution at 85 °C peaks at ≈550 nm while the same solution exhibits a dramatic redshift of ≈150 nm when cooled to room temperature, indicating that the polymer strongly aggregates in solution upon cooling. We found that when a single thiophene replaces the bithiophene linkages in the T3T backbone, the TDA property observed in solution of pristine T4T is reduced (Figure S1, Supporting Information) as the polymer is better solubilized.[26] By employing random polymerization in the preparation of conjugated terpolymers, self-aggregation can be tuned in solution and the melting point of the resulting D-A polymers is reduced.

To investigate the effect of the different polymer backbones on the optoelectronic properties of these materials, we compare the energy level and UV–vis absorption spectra of these films. Despite the difference in solution aggregation tendency for the five different polymers, all T4T derivatives were found

to have similar energy levels determined by the differential pulse voltammetry (DPV) and the onset wavelength of UV–vis absorption profile in our previous work, with an optical gap of ≈1.65 eV (Figure 1b), while T3T has slightly deeper lying highest occupied molecular orbital (HOMO) and lowest unoccupied molecular orbital (LUMO) levels with an optical gap ≈1.59 eV.[26] The absorption spectra of the pristine thin films, as well as polymer:IDTBR blends, are shown in Figure 1c,d respectively. The pristine polymer films exhibit similar absorption spectra with an absorption maximum at 700 nm, indicating that the structural modification in the copolymers does not significantly alter their optical properties. Finally, it is worth noting that both the donor polymers and IDTBR absorb in the range between 550–720 nm, and the spectral coverage of the blend films is narrow compared with $PC_{71}BM$ blends.[26] This lack of complementary absorption spectra is expected to limit the short-circuit current (J_{SC}) in the resulting devices compared to their fullerene counterparts.

To evaluate the photovoltaic performance and allow comparison to $PC_{71}BM$-based active layers, we blended these five polymers with IDTBR and fabricated inverted devices having the following architecture: ITO/ZnO/Donor polymer:IDTBR/MoO_x/Ag. The current density–voltage ($J–V$) characteristics of these devices are shown in **Figure 2**a and the photovoltaic device parameters are summarized in **Table 1**. The PffBT4T$_{90}$-co-3T$_{10}$:IDTBR device yielded the highest PCE of 8.7%, with a J_{SC} of 13.0 mA cm^{-2}, an open-circuit voltage (V_{OC}) of 1.07 V, and a fill factor (FF) of 63%. Figure 2b summarizes the device performance for
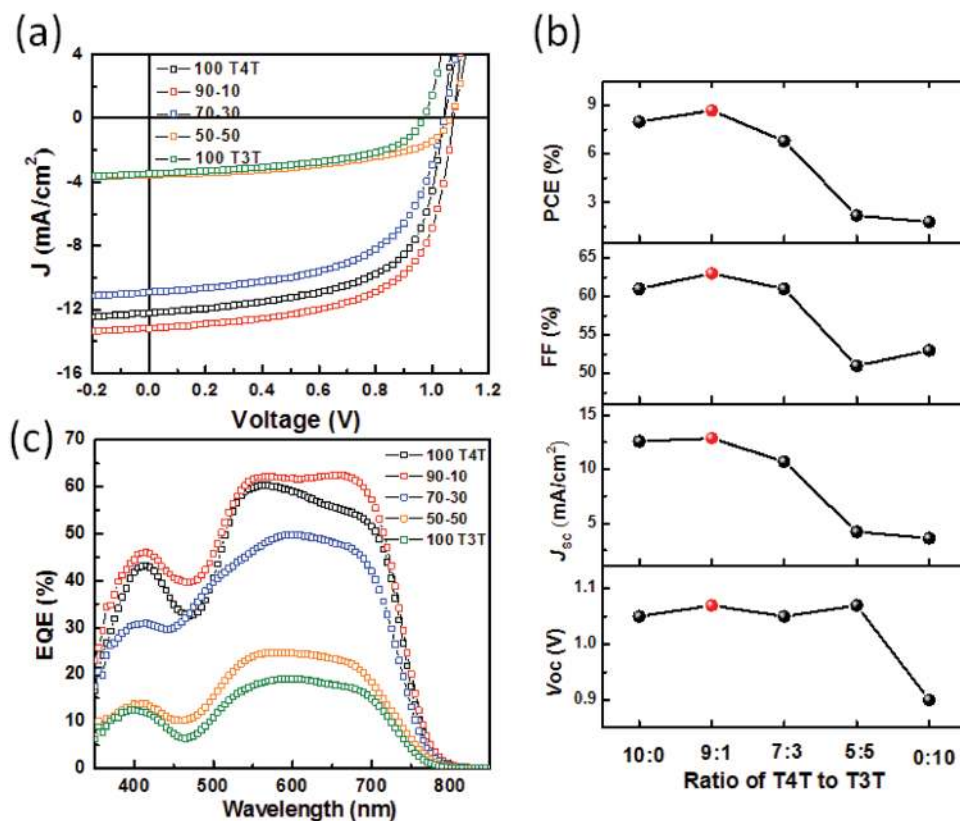

Figure 2. a) Current–voltage ($J–V$) curves of solar cells with different photoactive layers. b) Evolution of device performance as a function of the content of bithiophene linkers in the polymer backbone. c) External quantum efficiency (EQE) characteristics of solar cells.

**ADVANCED
SCIENCE NEWS**
www.advancedsciencenews.com

**ADVANCED
ENERGY
MATERIALS**
www.advenergymat.de

Table 1. Summary of device performance for solar cells based on polymer:IDTBR active layers.

Active layer	V_{OC} [V]	J_{SC} [mA cm^{-2}]	FF [%]	PCE [%]
PffBT4T-2OD:IDTBR	1.06 ± 0.01	12.6 ± 0.4	61 ± 1	8.0 ± 0.1
PffBT4T$_{90}$-co-3T$_{10}$: IDTBR	1.07 ± 0.01	13.0 ± 0.2	63 ± 1	8.7 ± 0.1
PffBT4T$_{70}$-co-3T$_{30}$: IDTBR	1.05 ± 0.03	10.7 ± 0.5	62 ± 2	6.8 ± 0.6
PffBT4T$_{50}$-co-3T$_{50}$: IDTBR	1.07 ± 0.01	4.2 ± 0.8	51 ± 1	2.2 ± 0.3
PffBT3T-2OD: IDTBR	0.91 ± 0.04	3.6 ± 0.3	52 ± 1	1.8 ± 0.2

the polymers with varying content of bithiophene linkers in the backbone. As shown in the figure, changing from pure T4T to PffBT4T$_{90}$-co-3T$_{10}$ results in an increase in both J_{SC} and FF. However, when the bithiophene content decreases to below 70%, the device PCE starts to drop until reaching 1.8% for the T3T:IDTBR devices. This decrease in device efficiency is caused primarily by a decrease in J_{SC}, which decreases from 13.0 mA cm^{-2} (PffBT4T$_{90}$-co-3T$_{10}$:IDTBR) to only 3.6 mA cm^{-2} (T3T:IDTBR), and a decrease in FF which decreases from 63% to 51%. To understand the origin of the large decrease in J_{SC}, external quantum efficiency (EQE) measurements were carried out and the results are shown in Figure 2c. Among all devices, the PffBT4T$_{90}$-co-3T$_{10}$:IDTBR devices show the highest EQE, with a flat photoresponse over 60% in the 550–700 nm wavelength range, which is consistent with the highest measured J_{SC} among the five devices. The overall EQE trend matches that of the J_{SC} with a noticeable decrease in quantum efficiency as the content of bithiophene linker decreases. To determine if this polymer-aggregation-dependent device performance is unique to IDTBR, we study the blends of the same five polymers with another NFA—ITIC-M. As shown in Figure S2 and

Table S1 (Supporting Information), the same trend is observed, which is the device performance decreases as thiophene linker content increases as a result of a decrease in both J_{SC} and FF. Here, the same trend with a different NFA indicates again that the aggregation properties of the polymer is important, suggesting that the aggregation properties of the donor polymer are the key factor determining the performance of NFA-based devices. Since there is not a decrease in device absorption as shown in Figure S3 (Supporting Information) our data suggest the decrease in EQE is due to either poor charge generation or poor charge transport in these devices, making this an excellent system for sorting out contributions from these two variables.

To understand the charge generation process in these devices, photoluminescence (PL) quenching measurements shown in **Figures 3**a–e were carried out, and the data used to determine whether exciton dissociation is the factor limiting charge generation processes in the devices with a low bithiophene content.[27–30] We found that both T4T and PffBT4T$_{90}$-co-3T$_{10}$ films exhibit strong PL quenching efficiencies of 70% and 88% respectively when blended with IDTBR. On the other hand, the PL quenching efficiencies are low for the other three blends (PffBT4T$_{70}$-co-3T$_{30}$, PffBT4T$_{50}$-co-3T$_{50}$, and T3T), which contain more single thiophene units. In the case of T3T:IDTBR, the quenching efficiency drops to as low as 38%. It is therefore apparent that in the PffBT4T$_{70}$-co-3T$_{30}$-, PffBT4T$_{50}$-co-3T$_{50}$-, and T3T-based devices, exciton dissociation is poor, leading to a low J_{SC}. Since the LUMO-LUMO offset between the donor polymer and IDTBR is similar for the terpolymer-based blends, we conclude that the low quenching efficiencies in the low-performance blends are due to the poor exciton dissociation efficiency, implying the low performance device is due to a problem in the blend film morphology.

To further investigate the charge generation dynamics in the films studied herein, transient PL measurements were also
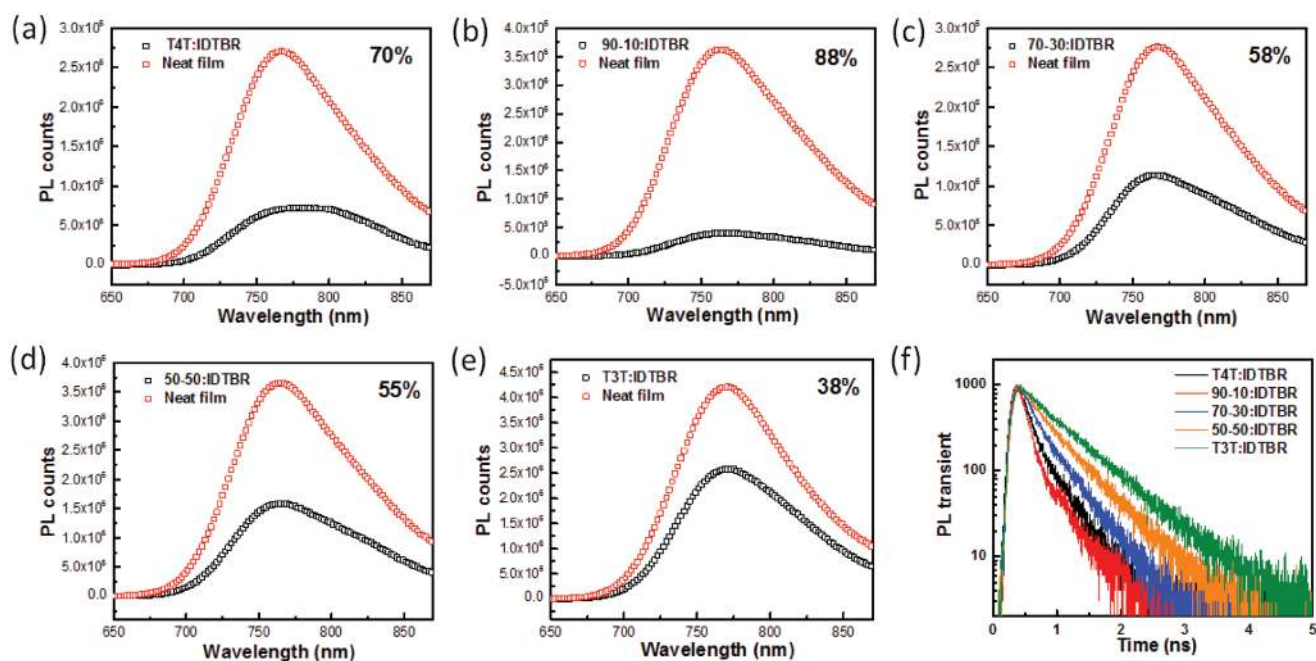

Figure 3. a–e) PL emission spectra for BHJ blend films and their corresponding pristine donor polymer film emissions. f) Transient PL decays for the BHJ blends.

carried out. It has been previously shown that in many cases when blending a polymer donor with an electron acceptor a biexponential decay is observed in the transient PL spectrum.[31] A fast initial decay on a sub-50 ps timescale is assigned to non-radiative decay of excitons to the charge-transfer (CT) states formed at the D-A interface, which in turn leads to fast exciton dissociation. A slower decay is due to exciton decay from excited states to ground states without charge transfer.[32,33] The transient PL data for the polymer:IDTBR films with different T4T to T3T ratios are shown in Figure 3f. As expected, all five blends have been found to have a much faster decay rate compared to the ≈1 ns single exponential decay in the pristine polymers (Figure S4, Supporting Information). A complete list of PL decay lifetimes is given in Table S2 (Supporting Information). In the case of the best performing PffBT4T$_{90}$-co-3T$_{10}$:IDTBR blends, the transient PL is characterized by a strong biexponential decay with a fast component lifetime of ≈2.8 ps, followed by a slow decay component with a lifetime of ≈99 ps. The fast-initial decay component accounted for 83% of the total decay and the slow decay component accounted for 17%. The T4T:IDTBR blend also exhibits a biexponential decay with a fast component lifetime of ≈3.6 ps (95%). Interestingly, the PL decays for PffBT4T$_{50}$-co-3T$_{50}$:IDTBR and T3T:IDTBR blends were characterized by a single exponential, with lifetimes of ≈288 and ≈405 ps respectively, which further supports our conjecture of low charge transfer efficiency in these blends, possibly due to a poor exciton dissociation efficiency resulted from a poor donor–acceptor interface.

We performed femtosecond transient absorption (TAS) measurements on the best-performing PffBT4T$_{90}$-co-3T$_{10}$:IDTBR blend and the worst-performing T3T:IDTBR blend to further quantitatively compare the charge generation dynamics between these films. Here, films are excited at 3 eV creating excitons and polarons in both donor and acceptor domains, as the polymer and IDTBR absorption spectra have a strong overlap. The subsequent exciton and polaron dynamics are tracked by measuring the differential transmittance of a broadband pulse in the IR region, and the corresponding TAS spectra of pristine polymer and blend films at different delays are shown in Figure S5 (Supporting Information). In the neat polymer TAS spectra, the negative bands centered around 0.9 and 1.2 eV are due to the excited state absorption of polymer singlet excitons and polarons in the charge-separated state, respectively, consistent

with the earlier results of TAS in PffBT4T-2OD polymers.[34] In the blend films, while the polymer exciton feature is easy to isolate from the TAS spectra at around 0.9 eV, the polaron generation and lifetime kinetics are harder to track because the photoinduced absorption (PIA) features of the polaron of the donor polymers and the PIA features of the exciton and polaron of the acceptor overlap significantly at ≈1.1 eV as shown in Figure S5 (Supporting Information). To compare the time evolution of excitons and polarons in different blends, we isolated individual contributions of these species by deconvoluting the spectra in the IR region using Gaussian fitting as shown in Figure S6 (Supporting Information). **Figure 4** shows the evolution of the singlet exciton decay and PIA signal at 1.1 eV in the neat and blend films obtained after deconvolution. As shown in Figure 4a, compared to the neat PffBT4T$_{90}$-co-3T$_{10}$ polymer film with a singlet exciton decay time of 95 ps, the singlet excitons of PffBT4T$_{90}$-co-3T$_{10}$:IDTBR films exhibit a shorter lifetime of 37 ps, indicating an efficient exciton splitting and electron transfer from the PffBT4T$_{90}$-co-3T$_{10}$ polymer to the acceptors. Moreover, the PffBT4T$_{90}$-co-3T$_{10}$:IDTBR blend shows a rise of the PIA signal at 1.1 eV, which is correlated with the exciton decay dynamics, indicating the rising feature probed at 1.1 eV is due to efficient polaron generation. On the other hand, the polaron population density increases as the excitation fluence increases as shown in Figure S7 (Supporting Information). By fitting to a multiexponential with time constants, we found the percentage of population of polaron rising signals increases from 16% at 5 uw to 25% at 10 uw and to 30% at 20 uw, and at the same time the percentage of depopulation of exciton fast-decaying features increase from 29% at 5 uw to 34% at 10 uw and to 47% at 20 uw. These observations indicate there is fast charge transfer from exciton to polaron excited states and singlet excitons can effectively separate regardless of initial excitation fluence. Different from the PffBT4T$_{90}$-co-3T$_{10}$:IDTBR blend, as shown in Figure 4b, pristine T3T and the T3T:IDTBR blend have similar exciton decay time of ≈100 ps, and there is a negligible rising polaron feature at 1.1 eV. These data again suggest that the dissociation of singlet excitons of T3T polymer is not efficient, limiting the charge generation process and resulting in a low short circuit current in T3T devices.

To understand why tuning the ratio between T4T and T3T in these polymers causes a dramatic difference in exciton dynamics, we investigate how the aggregation properties of
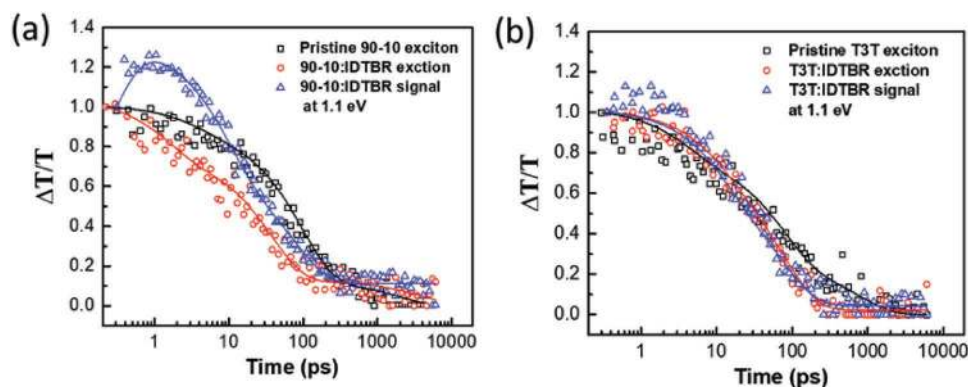

Figure 4. Normalized PIA dynamics of a) PffBT4T$_{90}$-co-3T$_{10}$ (90-10):IDTBR and b) PffBT3T-2OD (T3T):IDTBR.

ADVANCED
SCIENCE NEWS
www.advancedsciencenews.com

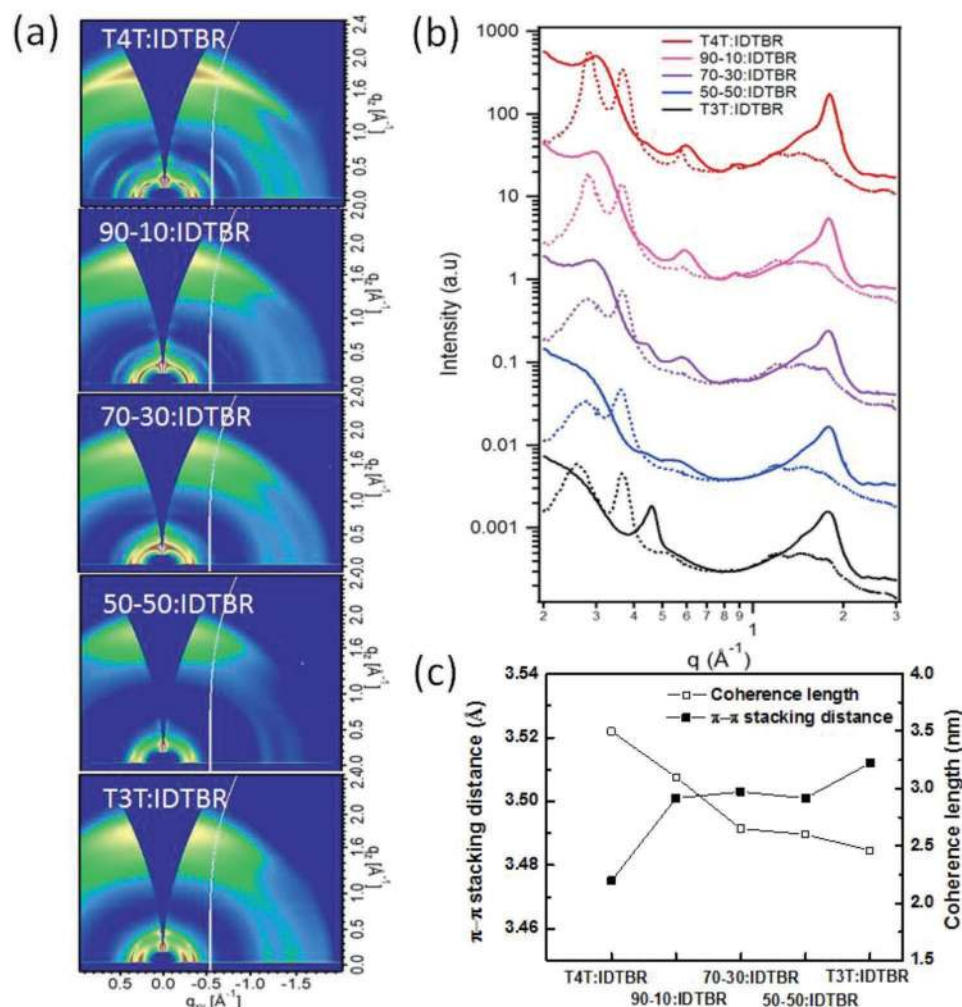**ADVANCED**
ENERGY
MATERIALS
www.advenergymat.de

Figure 5. a) 2D GIWAXS patterns of blend films. b) Out-of-plane (solid lines) and in-plane (dashed lines) 10° sector averaged GIWAXS profiles of blend films. c) Out-of-plane ($q_{xy} = 0$) π–π stacking distance and coherence lengths of the blend films.

the donor polymer influence molecular packing in the blends using grazing incidence wide angle X-ray scattering (GIWAXS). It should be noted that semicrystalline polymers typically organize into lamellar crystalline domains, having a face-to-face π–π stacking between backbones and lamellar stacking through the side chains.[35] Here, the pristine T4T and T3T polymers show well-defined lamellar peaks (100) at 0.28 Å^{-1} and π–π stacking peaks (010) at 1.78 Å^{-1} (Figure S8, Supporting Information). The intensities of the higher ordered peaks, (200) and (300), gradually decrease as the T3T units increase, indicating a reduction in long-range molecular order.[14] The corresponding 2D patterns of the blend films are shown in **Figure 5**a, and the out-of-plane and in-plane 1D GIWAXS profiles are depicted in Figure 5b. We found that all stacking peaks observed in the pristine polymer and IDTBR films are also observed in polymer:IDTBR blends, indicating that the polymers and the acceptor maintain their molecular packing in the blend. Looking at the molecular organization in the out-of-plane direction, we find that the (010) peak (the characteristic peak of π–π stacking) gradually shifts from 1.81 to 1.78 Å^{-1} as the bithiophene units are replaced by thiophene units (Figure 5c).

This peak shift corresponds to an increase in the π–π stacking distance from 3.47 to 3.51 Å as the aggregation tendency of the polymer decreases. A larger π–π distance in the out-of-plane direction is known to suppress the charge transport normal to the film as the barrier to hop from one chain to another is increased. At the same time, the π–π coherence length, which is quantified by the full width at half-maximum of the (010) diffraction peak via the Scherrer equation,[36] gradually decreases from 3.5 to 2.5 nm. Since the coherence length is an indication of the paracrystallinity,[37] the small coherence length of the T3T polymer plotted in Figure 5c indicates a decrease in the lattice ordering. Therefore, our GIWAXS results confirm our molecular structure design rationale, and polymer aggregation tendency indeed depends on the T4T/T3T unit ratio and influence the molecular packing in the ordered domains. Interestngly, we found an out-of-plane peak at ≈0.45 Å^{-1} and serveral off axis peaks in the T3T:IDTBR blend as shown in Figure 5b that are also observed in the solvent vapor annealed (SVA) pristine IDTBR film (Figure S9, Supporting Information) at the same position. As the SVA treatment is used to promote phase seperation and form highly crystalline domains, the appearance
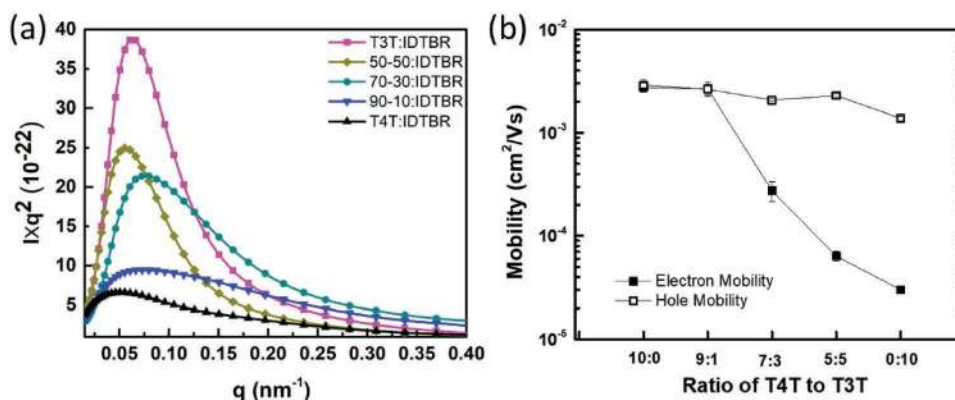
ADVANCED
SCIENCE NEWS
www.advancedsciencenews.com

ADVANCED
ENERGY
MATERIALS
www.advenergymat.de

Figure 6. a) Thickness normalized and Lorentz corrected R-SoXS profiles of blend films. b) Electron (solid squares) and hole (hollow squares) mobility of the polymer:IDTBR blends.

of the same peak in T3T:IDTBR as in an SVA IDTBR film indicates the formation of highly crystalline IDTBR domains and strong phase separation in the T3T:IDTBR blend relative to other four blend films where no out-of-plane peak at ≈0.45 Å^{-1} is observed.

Phase separation and underlying composition variations in D-A blends depend on the tendency to aggregate of the donor polymer and its miscibility with acceptors.[38] As supported by the GIWAXS data, the tendency of T4T to aggregate and order is gradually suppressed as the T4T:T3T ratio decreases. It is therefore expected that the five polymers investigated in this work will interact differently with IDTBR, resulting in a difference in the nanoscale morphology of these blends. To investigate the relationship between polymer aggregation and the blend morphology, we conducted Resonant Soft X-ray Scattering (R-SoXS) experiments. R-SoXS uses low energy X-rays with photon energies tuned to match the absorption edge of different chemical components. It is particularly sensitive when it comes to light elements like carbon, and thus R-SoXS can yield substantially improved signal-to-noise for organic materials.[39] As reported previously, the domain spacing and root-mean-square (RMS) composition variations (also referred to as average domain purity) extracted from R-SoXS are used to describe the length scale of composition variation and the extent of molecular mixing in the blends respectively.[40,41]

Figure 6a shows the R-SoXS profiles for all five blends. The well-defined peaks at low q (scattering vector in the reciprocal lattice) correspond to a domain size of ≈100 nm shown in all of the five blends. The domain size in these polymer:IDTBR blends is much larger than that in T4T:PC$_{71}$BM BHJs which was previously found to be in the range of 30–40 nm.[11] The origin of this difference may be related to the different aggregation properties between fullerene and IDTBR as well as the different miscibility between polymers and acceptors.[23,24,42] The apparent peak shoulder in the high q region shown in T4T and PffBT4T$_{90}$-co-3T$_{10}$ profiles suggests the multiscale morphologies with different-sized domains, indicating different film-formation processes involved.

To confirm the high q peak is not due to experimental artifact, we performed RSoXS experiments using three different energies of X-ray. As inferred from the energy dependent R-SoXS profiles (Figure S10, Supporting Information) of the T4T and PffBT4T$_{90}$-co-3T$_{10}$ blend films, both the high-q and low-q peaks exist when using three different x-ray energies, further confirming the presence of two domain-sizes.[43] With the multi-peak fitting for the T4T and PffBT4T$_{90}$-co-3T$_{10}$ blend films, in addition to the low q peaks, there are also relatively strong high q peaks at ≈0.17 nm^{-1} (Figure 6a, Table S3, Supporting Information) corresponding to another domain size of ≈40 nm. It should be noted that the high q peaks in the other three blends (PffBT4T$_{70}$-co-3T$_{30}$: IDTBR, PffBT4T$_{50}$-co-3T$_{50}$: IDTBR, and T3T: IDTBR) decreases as the T4T/T3T ratio decreases. To fully understand the morphology, multiple peak fitting was used to quantitatively analyze the data and the results for low-q and high-q peaks are summarized in **Table 2**. As shown in Table 2, the PffBT4T$_{90}$-co-3T$_{10}$ blend films have the largest relative volume fraction of small domains among all of five blended films with ≈28% of domains smaller than 40 nm (assuming that the composition of the domains remains the same). Generally, higher relative volume fraction of small domains leads to a higher device fill factor and short-circuit current, as the D-A interfacial area is maximized, which in turn facilitates efficient exciton dissociation and charge generation.[43,44] The results suggest that the formation of small domains in PffBT4T$_{90}$-co-3T$_{10}$:IDTBR films is one of the main reasons for the high J_{SC} in

Table 2. Summary of root-mean-square composition variation and average domain spacing obtained from the R-SoXS analysis.

Materials	Domain spacing for low-q peak [nm]	Domain spacing for high-q peak [nm]	Overall RMS composition variation	Volume fraction of high-q peak [%]
PffBT4T-2OD:IDTBR	129.5	32.5	0.52	19
PffBT4T$_{90}$-co-3T$_{10}$: IDTBR	97.4	37.2	0.66	28
PffBT4T$_{70}$-co-3T$_{30}$: IDTBR	85.4	39.8	0.75	3
PffBT4T$_{50}$-co-3T$_{50}$: IDTBR	110.5	31.0	0.83	4
PffBT3T-2OD: IDTBR	98.4	34.0	1	6

these devices. In the case of T4T:IDTBR films, only 19% of the domains are small, and thus devices exhibit a slightly lower J_{SC} and FF compared to PffBT4T$_{90}$-co-3T$_{10}$.IDTBR devices.

Root-mean-square (RMS) composition variations derived from the R-SoXS data is proportional to the square-root of normalized integrated scattering intensity, indicative of the average purity of mixed donor and acceptor regions.[45,46] A large relative RMS composition variation is a characteristic of the presence of more pure domains compared to a small RMS composition variation.[36] It is known that high-aggregated polymer can maintain its crystallinity when blended with acceptors, resulting in a high domain purity.[47,48] On the contrary, we observed an opposite trend, as summarized in Table 2, the RMS composition variation of the T4T:IDTBR blend is 0.52, compared to 1 for the T3T:IDTBR blend, indicating as the aggregation tendency decreases from pure T4T to pure T3T, the domain purity increases approximately 2 times. To understand the differences in domain purity, we quantify donor–acceptor interaction parameter (χ) using differential scanning calorimetry (DSC) as shown in Figure S11 (Supporting Information). The χ parameter, providing important information associated with the miscibility of donor and acceptor, is quantified according to the Nishi–Wang equation[49] (details are shown in the Supporting Information). The χ parameters are different for different systems: 0.6 for T4T:IDTBR, 0.5 for PffBT4T$_{90}$-co-3T$_{10}$:IDTBR, 0.8 for PffBT4T$_{50}$-co-3T$_{50}$:IDTBR and 0.9 for T3T:IDTBR. From the previous results, the highest χ value of the T3T system is an indication for poor miscibility and strong tendency for phase separation and the lowest χ value of the PffBT4T$_{90}$-co-3T$_{10}$ system is an indication for high donor–acceptor miscibility resulting in well-mixed domains with less purity as observed in R-SoXS results.[22,41,46] Generally, photocurrent generation is strongly influenced by the exciton dissociation efficiency in the mixed domains.[50] The ideal mixed domain should be a finely dispersed blend of the donor polymer with the NFA molecules to facilitate charge generation and exciton dissociation.[51,52] The low purity of PffBT4T$_{90}$-co-3T$_{10}$ and T4T blend domains, as a result of high miscibility with IDTBR is probably the reason for efficient charge generation, leading to a substantially higher J_{SC} compared to the T3T blend.[20]

In addition to charge generation, the aggregation properties and molecular packing of donor polymers are expected to also affect the formation of percolation pathways for charge extraction. To understand the influence of donor polymer aggregation on charge transport, we measure the space charge limited current (SCLC) charge carrier mobility for holes and electrons in the polymer:IDTBR blends. As shown in Figure 6b, hole mobilities for all blends are relatively high, on the order of 10^{-3} cm^2 V^{-1} s^{-1}, with a slight downward trend observed from pure T4T to pure T3T. The high hole mobility indicates efficient hole transport in all bend films resulting from the crystalline domains and short π–π distance. Different from the hole mobility, the blend electron mobility shows a strong dependence on donor polymers. The electron mobility for the T4T and PffBT4T$_{90}$-co-3T$_{10}$ blends is comparable to their hole mobility, which both are on the order of 10^{-3} cm^2 V^{-1} s^{-1}. Both the electron and hole mobilities are well-balanced in these blends, and therefore the charge extraction is expected to be efficient. However, when going from PffBT4T$_{90}$-co-3T$_{10}$ to PffBT4T$_{70}$-co-3T$_{30}$, the electron mobility drops by one order of magnitude

to $\approx 10^{-4}$ cm^2 V^{-1} s^{-1} and continuously drops further to $\approx 10^{-5}$ cm^2 V^{-1} s^{-1} in T3T:IDTBR blends. The low electron mobility in the PffBT4T$_{50}$-co-3T$_{50}$:IDTBR and T3T:IDTBR blends does not come as a surprise since the large (≈ 100 nm) and pure domains forming in these active layers are expected to inhibit the formation of continuous percolating IDTBR pathways for electrons to hop through, and therefore electron mobility is expected to be low.[51] The low electron mobility, in addition to low exciton dissociation efficiency in PffBT4T$_{50}$-co-3T$_{50}$:IDTBR and T3T:IDTBR devices are considered to be the reasons for the low J_{SC} and FF measured in these devices.

Insight into the origin of the polymer aggregation dependence of BHJ morphology and device performance of five donor polymers is obtained through high speed in situ UV–vis absorbance measurements performed during the spin-coating process with a 50 ms time resolution.[53–55] The UV–vis absorbance spectra of both pristine materials and donor–acceptor blends recorded at different times during spin-coating are shown in Figure S12 (Supporting Information). Basically, the evolution of absorbance signal can be roughly divided into three stages according to the relative positions of various vibronic peaks of polymer and IDTBR.[54] As shown in Figure S12 (Supporting Information), in the first stage, there is a rapid decrease of the absorbance intensity without a peak shift, indicating no interactions or ordering processes, which denotes thinning due to outflow and free solvent evaporation without aggregation. In the second stage, after the absorbance reaches a minimum value, a distinct redshift arises as time elapses as a result of aggregation of molecules/polymer chains. In the final stage, the molecular chains are frozen as the material solidifies and ceases to evolve and the absorbance spectra are commensurately constant with time. Here, we are more interested in the second stage as it provides important insight into the sequence of aggregation and the aggregation kinetics of the BHJ components in neat and blend films. To be specific, the two vibronic peaks of T4T polymer shift, respectively, from 400 and 560 to 450 and 680 nm. Similarly, the vibronic peaks of the PffBT4T$_{90}$-co-3T$_{10}$ polymer shift, respectively, from 400 and 560 to 440 and 680 nm, while the vibronic peaks of the PffBT4T$_{50}$-co-3T$_{50}$ polymer shift, respectively, from 400 and 560 to 430 and 680 nm. Similarly, the neat acceptor IDTBR film also shows the main peak shift from 650 to 680 nm, with a key difference from polymer's aggregation signature is the absence of a redshift of the 400 nm peak. As a result, the absorbance at ≈ 450 nm in the blend solution can be ascribed to the polymer aggregation and the absorbance at 680 nm is likely due to both polymer and IDTBR aggregation. To investigate the aggregation kinetics, we track the evolutions of the absorbance at ≈ 450 and 680 nm for the blends as well as the pristine donor and acceptor materials, as shown in **Figure 7**. The materials aggregation kinetics, characterized by the step-like increase in the absorbance in the second stage, are visibly different across the different polymer:IDTBR blends. As shown in Figure 7, in the highly aggregated T4T and PffBT4T$_{90}$-co-3T$_{10}$ blend solution, both the 450 and 680 nm peaks arise at an onset of ≈ 3 s, lasting only ≈ 150 ms, consistent with the neat polymer aggregation onset which also starts at ≈ 3 s, much earlier than the aggregation of neat IDTBR, which starts a second later (≈ 4 s). The similarity of the aggregation dynamics of the neat polymer and

ADVANCED
SCIENCE NEWS
www.advancedsciencenews.com

ADVANCED
ENERGY
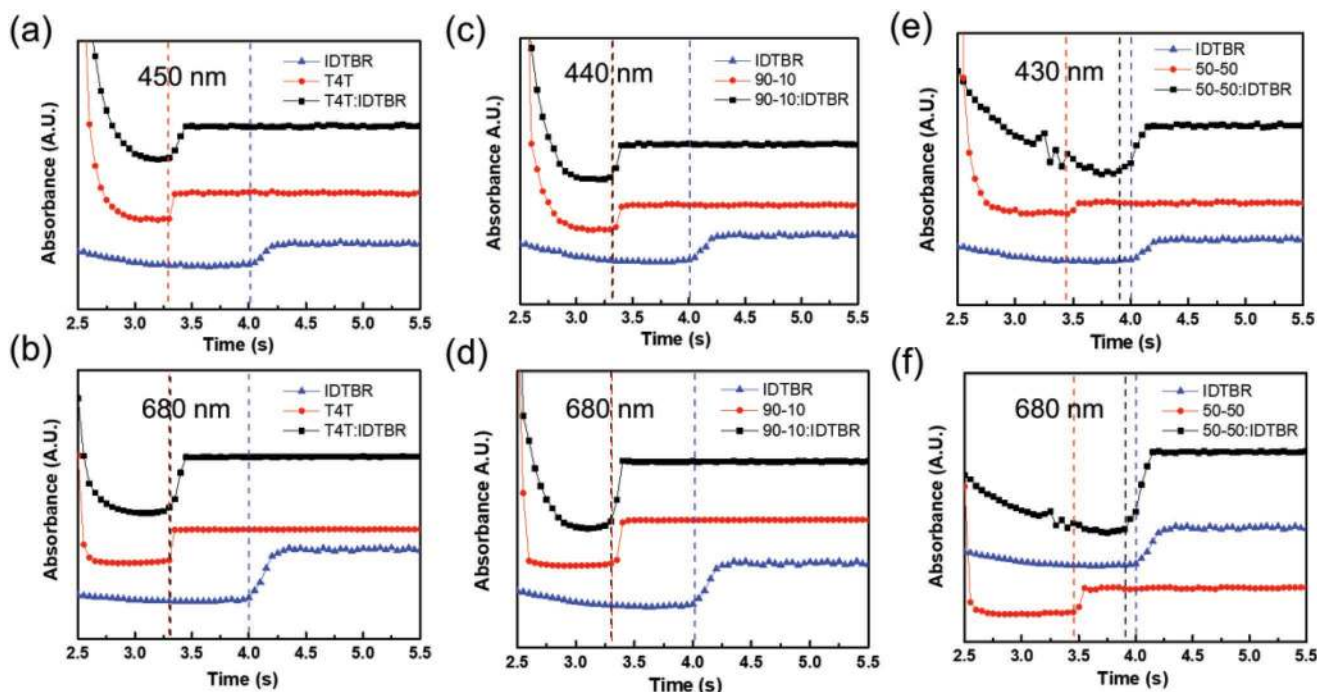**MATERIALS**
www.advenergymat.de

Figure 7. Time evolution of the intermolecular aggregation peaks during spin-coating for neat and blend solutions. a) T4T systems at 450 nm. b) T4T systems at 680 nm. c) PffBT4T$_{90}$-co-3T$_{10}$ systems at 440 nm. d) PffBT4T$_{90}$-co-3T$_{10}$ systems at 680 nm. e) PffBT4T$_{50}$-co-3T$_{50}$ systems at 430 nm. f) PffBT4T$_{50}$-co-3T$_{50}$ systems at 680 nm.

the blend indicates fast polymer aggregation is dominant at the early stage of the donor–acceptor solution drying process, due to the limited solubility of the polymer causing liquid–solid phase separation.[56,57] We note that the redshift of the IDTBR vibronic peak overlaps with the polymer aggregation signature, to isolate the IDTBR aggregation kinetics in the following liquid–liquid phase separation, led by donor–acceptor interaction at the solvent evaporation crosses the binodal,[58] require more detail data analysis. Considering the high miscibility of T4T/PffBT4T$_{90}$-co-3T$_{10}$ with IDTBR, we propose IDTBR aggregation is suppressed during the following liquid–liquid phase separation, resulting in well-mixed domains as observed from R-SoXS. Different from highly aggregated polymer systems, during spin-coating, aggregation is much slower in the less-aggregated PffBT4T$_{50}$-co-3T$_{50}$:IDTBR blend solutions starting at approximately ≈3 s and lasting ≈250 ms, similar to neat IDTBR drying kinetics. The slow aggregation onset suggests that, in the PffBT4T$_{50}$-co-3T$_{50}$:IDTBR solution, the initial liquid–solid phase separation is suppressed and liquid–liquid phase separation dominant in the final film drying process, resulting in isolated large-sized domains with high-purity.[57]

In summary, we have shown that the differences in aggregation and nanoscale morphology between five polymers having similar backbones are responsible for vastly different device performance when blended with IDTBR. From our results, we have shown that polymer aggregation and miscibility with NFA control the domain size and purity, dictating the charge generation and transport in these BHJs. Specifically, we show that T4T, having a strong aggregation tendency in solution, results in a better device performance compared to T3T which has a low tendency to aggregate. Furthermore, from in

situ UV–vis measurements, we observe that the rapid T4T and PffBT4T$_{90}$-co-3T$_{10}$ polymer aggregation happens prior to the liquid–liquid phase separation in blends, resulting in a high-fraction of 30–40 nm small domains derived from the R-SoXS data. Additionally, their high miscibility (low χ) with IDTBR suppresses phase separation, resulting in relatively mixed domains, which promote exciton dissociation and carrier transport in polymer:IDTBR blends. In contrast, we found the aggregation process of donor polymer slowed down in the less-aggregated polymer:IDTBR blends, and the poor miscibility (high χ) between T3T and IDTBR leads to a strong liquid–liquid phase separation, resulting in the formation of high-purified domains, inhibiting exciton dissociation and charge carrier transport. Our best performing polymer, PffBT4T$_{90}$-co-3T$_{10}$, benefits from polymer aggregation and mixed domains, while the addition of less-aggregated T3T units disrupt strong π–π interaction and result in the formation of a higher volume fraction of smaller-sized domains which further promote carrier generation and transport. A schematic highlighting the film formation process for PffBT4T-2OD:IDTBR, PffBT4T$_{90}$-co-3T$_{10}$:IDTBR, and PffBT3T-2OD:IDTBR along with the morphologies is shown in **Figure 8**. It is likely that the performance of the PffBT3T-2OD:IDTBR could be improved if an additive were to be found and used that allowed to quench the composition of the mixed domains to be closer to the percolation threshold.[59,60]

3. Conclusion

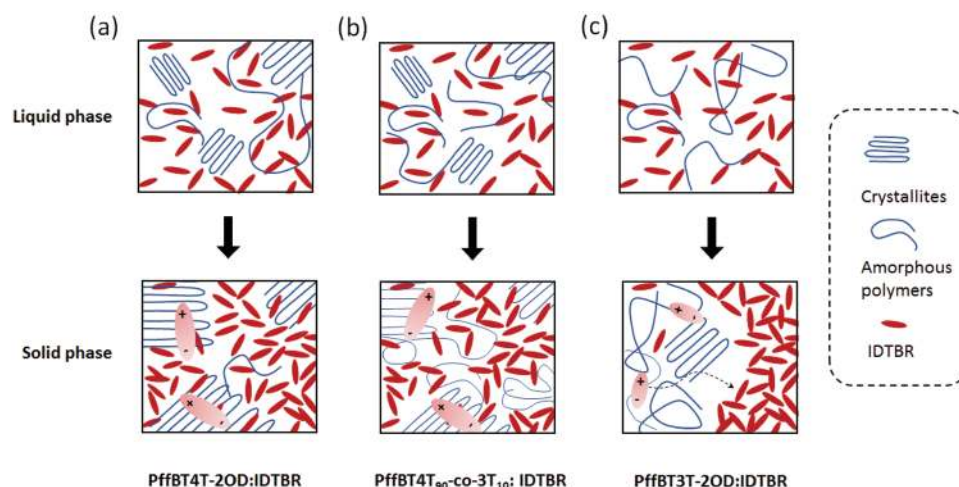In this work we systematically compared the photovoltaic performance of a family of donor polymers derived from

Figure 8. Morphology evolution during drying for T4T, PffBT4T$_{90}$-*co*-3T$_{10}$, and T3T in blends with IDTBR.

PffBT4T-2OD by varying the ratio of bithiophene to thiophene. Despite their similar energy levels and optical properties, these polymers exhibit very different aggregation properties and molecular packing. Here, we found that polymers with a strong temperature-dependent-aggregation property, T4T and PffBT4T$_{90}$-*co*-3T$_{10}$, yield better-performing devices when blended with IDTBR compared to the other three polymers. GIWAXS confirmed a gradual decrease in coherence length and a gradual increase in the π–π stacking distance when bithiophene is replaced with thiophene. Additionally, results from In situ UV–vis, R-SoXS and DSC measurements showed that multiscale domains are formed due to polymer aggregation prior to liquid–liquid phase separation, and domain purity decreases with increased miscibility. Strong donor–acceptor phase separation in PffBT4T$_{70}$-*co*-3T$_{30}$:IDTBR, PffBT4T$_{50}$-*co*-3T$_{50}$:IDTBR and T3T:IDTBR films significantly suppresses exciton dissociation and transport reflected in our mobility measurements. In the T4T and PffBT4T$_{90}$-*co*-3T$_{10}$ blends having a multiscale morphology, the PL quenching and exciton dissociation efficiency remained high, signifying a high charge generation efficiency. This work illustrates how the aggregation property of the donor polymer influences phase separation and the corresponding exciton and charge kinetics in polymer/NFA blends.

4. Experimental Section

Materials: PffBT4T-2OD, PffBT3T-2OD, PffBT4T$_{90}$-*co*-3T$_{10}$, PffBT4T$_{70}$-*co*-3T$_{30}$, and PffBT4T$_{50}$-*co*-3T$_{50}$ were synthesized as described previously.[26] IDTBR was purchased from 1-Material.

Device Fabrication: The BHJ devices were fabricated with the inverted structure: glass/ITO/ZnO/Active layer/MoO$_x$/Ag. Patterned ITO glass was precleaned in acetone and isopropanol. A thin layer of ZnO sol-gel was spin-coated (4000 rpm) onto the glass and baked at 150 °C for 30 min. The active layer solutions (13 mg mL^{-1}) of donor polymer: IDTBR (1:1.2 weight ratio) were dissolved in chlorobenzene (CB). Both the solution and substrates were preheated at 100 °C. Active layers were spin-coated at hot solution and hot substrates condition and at 1500 rpm to get an active layer of ≈90 nm. The substrates were then transferred into the evaporation chamber. Thermal evaporation was used for the deposition of 8 nm MoO$_x$ and 100 nm of Ag at a pressure of ≈1 × 10^{-6} torr.

Device Characterization: J-V characteristics were acquired using a Keithley 4200 semiconductor parameter analyzer along with a Newport Thermal Oriel 94021 1000 W solar simulator, at 100 mW cm^{-2} incident power. EQE measurements were conducted using an in-house setup consisting of a Xenon DC arc lamp, an ORIEL 74125 monochromator, a Keithley 428 current amplifier, an SR 540 chopper system and an SR830 DSP lock-in amplifier from SRS. Films absorbance measurements were made with a Perkins Elmer UV–vis spectrometer.

Photoluminescence (PL): Time-resolved PL measurements were performed at the NCSU Imaging and Kinetic Spectroscopy (IMAKS) Laboratory in the Department of Chemistry. The PL decays were measured using a time-correlated single photon counting (TCSPC) spectrometer (LifeSpec II, Edinburgh Instruments, IRF ≈ 100 ps), described previously.[61] Chameleon Ultra II Ti:Sapphire oscillator (Coherent) was used as the light source. The output of the laser (≈50 nJ per pulse, 140 fs at 800 nm, 80 MHz repetition rate) was passed through a pulse picker (9200, Coherent) to reduce the repetition rate to 4 MHz and through a frequency doubler (fs-SHG, A.P.E.) to generate a UV excitation pulse, re-collimated, and directed into the TCSPC spectrometer. The PL was collected in 90° geometry. The instrument response function was measured using scattered light from a microscope slide.

Transient Absorption Spectroscopy: Transient absorption data were collected using transient absorption spectroscopy setup. This setup consists of the spectrometer (Ultrafast Helios system) and amplified Ti:Sapphire Laser. The output of amplified Ti:Sapphire Laser provides 800 nm fundamental pulses at 1 kHz repetition rate which were split into two optical beams to generate pump and probe pulses. One fundamental beam was used to generate pump beam using an optical parametric amplifier (OPA) system (Coherent Opera Solo). A white light/NIR probe was generated by focusing another fundamental beam into a flint glass. Pump and probe beams were focused on a sample and probe light was collected by a charge-coupled device CCD device. The spectral detection region was 0.8 eV to 1.6 eV. The thin film samples were encapsulated using UV curable clue before measurement. The instrument response function (IRF) was ≈100 fs full-width at half-maximum. The samples were excited with the excitation energy 2.68 eV for acceptor excitation and 1.75 eV for the donor excitation and the fractional change in transmission was detected in the probe range 0.8-1.6 eV at several time delays.

GIWAXS and R-SoXS: GIWAXS and R-SoXS were respectively performed at the beamline 7.3.3[62] and beamline 11.0.1.2[63] Advanced Light Source (ALS), Lawrence Berkeley National Laboratory, following the previously established protocols. GIWAXS data were acquired just above the critical angle (0.13°) of the films with a hard X-ray energy of 10 keV, and Silver Behenate (AgB) was used for geometry calibration.

R-SoXS was performed in a transmission geometry with linearly polarized photons under high vacuum (1×10^{-7} torr) and a cooled (−45 °C) CCD (Princeton PI-MTE, 2048 pixels × 2048 pixels) was used to capture the soft X-ray scattering 2D maps and PS300 was used for geometry calibration.

In Situ Optical Measurements: In situ UV–vis was performed using a F20-UVX spectrometer (Filmetrics, Inc.) equipped with tungsten halogen and deuterium light sources (Filmetrics, Inc.) over the wavelength range of interest from 300 nm to 1000 nm. Most measurements were performed with an integration time of 0.05 s per absorption spectrum. The solution concentration and spin-coating parameters were as same as those used while fabricating devices to keep consistent. Time zero was selected when spin-coating was started. The time lag between solution drop and measurement starting was about 2 s.

Supporting Information

Supporting Information is available from the Wiley Online Library or from the author.

Conflict of Interest

The authors declare no conflict of interest.

[1] L. Meng, Y. Zhang, X. Wan, C. Li, X. Zhang, Y. Wang, X. Ke, Z. Xiao, L. Ding, R. Xia, H. Yip, Y. Cao, Y. Chen, *Science* **2018**, *361*, 1094.

[2] N. Liang, W. Jiang, J. Hou, Z. Wang, *Mater. Chem. Front.* **2017**, *1*, 1291.

[3] J. Zhang, H. S. Tan, X. Guo, A. Facchetti, H. Yan, *Nat. Energy* **2018**, *3*, 720.

[4] N. Gasparini, M. Salvador, S. Strohm, T. Heumueller, I. Levchuk, A. Wadsworth, J. H. Bannock, J. C. de Mello, H. J. Egelhaaf, D. Baran, I. McCulloch, C. J. Brabec, *Adv. Energy Mater.* **2017**, *7*, 1700770.

[5] J. Hou, O. Inganas, R. H. Friend, F. Gao, *Nat. Mater.* **2018**, *17*, 119.

[6] G. Yu, J. Gao, J. C. Hummelen, F. Wudl, A. J. Heeger, *Science* **1995**, *270*, 1789.

[7] A. J. Heeger, *Adv. Mater.* **2014**, *26*, 10.

[8] G. Dennler, M. C. Scharber, C. J. Brabec, *Adv. Mater.* **2009**, *21*, 1323.

[9] R. Noriega, J. Rivnay, K. Vandewal, F. P. V Koch, N. Stingelin, P. Smith, M. F. Toney, A. Salleo, *Nat. Mater.* **2013**, *12*, 1038.

[10] H. Hu, P. C. Y. Chow, G. Zhang, T. Ma, J. Liu, G. Yang, H. Yan, *Acc. Chem. Res.* **2017**, *50*, 2519.

[11] Y. Liu, J. Zhao, Z. Li, C. Mu, W. Ma, H. Hu, K. Jiang, H. Lin, H. Ade, H. Yan, *Nat. Commun.* **2014**, *5*, 5293.

[12] T. Heumueller, W. R. Mateker, I. T. Sachs-quintana, K. Vandewal, J. A. Bartelt, T. M. Burke, T. Ameri, J. Brabec, M. D. Mcgehee, *Energy Environ. Sci.* **2014**, *7*, 2974.

[13] H. Kang, M. A. Uddin, C. Lee, K. H. Kim, T. L. Nguyen, W. Lee, Y. Li, C. Wang, H. Y. Woo, B. J. Kim, *J. Am. Chem. Soc.* **2015**, *137*, 2359.

[14] Z. Li, K. Jiang, G. Yang, J. Y. L. Lai, T. Ma, J. Zhao, W. Ma, H. Yan, *Nat. Commun.* **2016**, *7*, 13094.

[15] S. Ko, Q. V. Hoang, C. E. Song, M. A. Uddin, E. Lim, S. Y. Park, B. H. Lee, S. Song, S. Moon, S. Hwang, P. Morin, M. Leclerc, G. M. Su, M. L. Chabinyc, H. Y. Woo, W. S. Shin, J. Y. Kim, *Energy Environ. Sci.* **2017**, *10*, 1443.

[16] N. D. Eastham, A. S. Dudnik, T. J. Aldrich, E. F. Manley, T. J. Fauvell, P. E. Hartnett, M. R. Wasielewski, L. X. Chen, F. S. Melkonyan, A. Facchetti, R. P. H. Chang, T. J. Marks, *Chem. Mater.* **2017**, *29*, 4432.

[17] K. W. Chou, B. Yan, R. Li, E. Q. Li, K. Zhao, D. H. Anjum, S. Alvarez, R. Gassaway, A. Biocca, S. T. Thoroddsen, A. Hexemer, A. Amassian, *Adv. Mater.* **2013**, *25*, 1923.

[18] C. Schünemann, D. Wynands, L. Wilde, M. P. Hein, S. Pfützner, C. Elschner, K. J. Eichhorn, K. Leo, M. Riede, *Phys. Rev. B* **2012**, *85*, 245314.

[19] L. Ye, B. A. Collins, X. Jiao, J. Zhao, H. Yan, H. Ade, *Adv. Energy Mater.* **2018**, *8*, 1703058.

[20] L. Ye, H. Hu, M. Ghasemi, T. Wang, B. A. Collins, J. H. Kim, K. Jiang, J. H. Carpenter, H. Li, Z. Li, T. McAfee, J. Zhao, X. Chen, J. L. Y. Lai, T. Ma, J. L. Bredas, H. Yan, H. Ade, *Nat. Mater.* **2018**, *17*, 253.

[21] T. Wang, A. J. Pearson, D. G. Lidzey, *J. Mater. Chem. C* **2013**, *1*, 7266.

[22] L. Ye, B. A. Collins, X. Jiao, J. Zhao, H. Yan, H. Ade, *Adv. Energy Mater.* **2018**, *8*, 1870124.

[23] H. B. Naveed, W. Ma, *Joule* **2018**, *2*, 621.

[24] K. Jiang, G. Zhang, G. Yang, J. Zhang, Z. Li, T. Ma, H. Hu, W. Ma, H. Ade, H. Yan, *Adv. Energy Mater.* **2018**, *8*, 1701370.

[25] X. Yi, B. Gautam, I. Constantinou, Y. Cheng, Z. Peng, E. Klump, X. Ba, C. H. Y. Ho, C. Dong, S. R. Marder, J. R. Reynolds, S. W. Tsang, H. Ade, F. So, *Adv. Funct. Mater.* **2018**, *28*, 1802702.

[26] B. Xu, I. Pelse, S. Agarkar, S. Ito, J. Zhang, X. Yi, Y. Chujo, S. Marder, F. So, J. R. Reynolds, *ACS Appl. Mater. Interfaces* **2018**, *10*, 44583.

[27] L. Lu, T. Xu, W. Chen, E. S. Landry, L. Yu, *Nat. Photonics* **2014**, *8*, 716.

[28] H. Hoppe, M. Niggemann, C. Winder, J. Kraut, R. Hiesgen, A. Hinsch, D. Meissner, N. S. Sariciftci, *Adv. Funct. Mater.* **2004**, *14*, 1005.

[29] D. Veldman, Ö. Ipek, S. C. J. Meskers, J. Sweelssen, M. M. Koetse, S. C. Veenstra, J. M. Kroon, S. S. Van Bavel, J. Loos, R. A. J. Janssen, *J. Am. Chem. Soc.* **2008**, *130*, 7721.

[30] C. Piliego, M. A. Loi, *J. Mater. Chem.* **2012**, *22*, 4141.

[31] T. H. Lai, I. Constantinou, C. M. Grand, E. D. Klump, S. Baek, H. Y. Hsu, S. W. Tsang, K. S. Schanze, J. R. Reynolds, F. So, *Chem. Mater.* **2016**, *28*, 2433.

[32] B. Bernardo, D. Cheyns, B. Verreet, R. D. Schaller, B. P. Rand, N. C. Giebink, *Nat. Commun.* **2014**, *5*, 3245.

[33] I. Constantinou, X. Yi, N. T. Shewmon, E. D. Klump, C. Peng, S. Garakyaraghi, C. K. Lo, J. R. Reynolds, F. N. Castellano, F. So, *Adv. Energy Mater.* **2017**, *7*, 1601947.

[34] B. R. Gautam, R. Younts, J. Carpenter, H. Ade, K. Gundogdu, *J. Phys. Chem. A* **2018**, *122*, 3764.

[35] Y. H. Lin, K. G. Yager, B. Stewart, R. Verduzco, *Soft Matter* **2014**, *10*, 3817.

[36] L. Ye, W. Zhao, S. Li, S. Mukherjee, J. H. Carpenter, O. Awartani, X. Jiao, J. Hou, H. Ade, *Adv. Energy Mater.* **2017**, *7*, 1602000.

[37] J. Rivnay, R. Noriega, R. J. Kline, A. Salleo, M. F. Toney, *Phys. Rev. B* **2011**, *84*, 045203.

[38] M. T. Weintraub, E. Xhakaj, A. Austin, J. M. Szarko, *J. Mater. Chem. C* **2016**, *4*, 7756.

[39] X. Jiao, L. Ye, H. Ade, *Adv. Energy Mater.* **2017**, *7*, 1700084.

[40] L. Ye, X. Jiao, S. Zhang, H. Yao, Y. Qin, H. Ade, J. Hou, *Adv. Energy Mater.* **2017**, *7*, 1601138.

[41] H. Hu, Y. Li, J. Zhang, Z. Peng, L. Ma, J. Xin, J. Huang, T. Ma, K. Jiang, G. Zhang, W. Ma, H. Ade, H. Yan, *Adv. Energy Mater.* **2018**, *8*, 1800234.

[42] H. Cha, J. Wu, A. Wadsworth, J. Nagitta, S. Limbu, S. Pont, Z. Li, J. Searle, M. F. Wyatt, D. Baran, J. S. Kim, I. McCulloch, J. R. Durrant, *Adv. Mater.* **2017**, *29*, 1701156.

[43] L. Ye, Y. Xiong, S. Li, M. Ghasemi, N. Balar, J. Turner, A. Gadisa, J. Hou, B. T. O'Connor, H. Ade, *Adv. Funct. Mater.* **2017**, *27*, 1702016.

[44] H. Zhang, X. Wang, L. Yang, S. Zhang, Y. Zhang, C. He, W. Ma, J. Hou, *Adv. Mater.* **2017**, *29*, 1703777.

[45] H. Ade, A. P. Hitchcock, *Polymer* **2008**, *49*, 643.

[46] L. Ye, X. Jiao, W. Zhao, S. Zhang, H. Yao, S. Li, H. Ade, J. Hou, *Chem. Mater.* **2016**, *28*, 6178.

[47] S. Venkatesan, J. Chen, E. C. Ngo, *Nano Energy* **2015**, *12*, 457.

[48] B. P. Lyons, N. Clarke, C. Groves, *Energy Environ. Sci.* **2012**, *5*, 7657.

[49] T. Nishi, T. T. Wang, *Macromolecules* **1975**, *8*, 909.

[50] C. Zhang, T. Heumueller, W. Gruber, O. Almora, X. Du, L. Ying, J. Chen, T. Unruh, Y. Cao, N. Li, C. J. Brabec, *ACS Appl. Mater. Interfaces* **2019**, *11*, 18555.

[51] J. A. Bartelt, Z. M. Beiley, E. T. Hoke, W. R. Mateker, J. D. Douglas, B. A. Collins, J. R. Tumbleston, K. R. Graham, A. Amassian, H. Ade, J. M. J. Fréchet, M. F. Toney, M. D. Mcgehee, *Adv. Energy Mater.* **2013**, *3*, 364.

[52] N. Li, J. D. Perea, T. Kassar, M. Richter, T. Heumueller, G. J. Matt, Y. Hou, N. S. Güldal, H. Chen, S. Chen, S. Langner, M. Berlinghof, T. Unruh, C. J. Brabec, *Nat. Commun.* **2017**, *8*, 14541.

[53] H. W. Ro, J. M. Downing, S. Engmann, A. A. Herzing, D. M. Delongchamp, L. J. Richter, S. Mukherjee, H. Ade, M. Abdelsamie, L. K. Jagadamma, A. Amassian, Y. Liu, H. Yan, *Energy Environ. Sci.* **2016**, *9*, 2835.

[54] Y. Mao, W. Li, M. Chen, X. Chen, R. S. Gurney, D. Liu, T. Wang, *Mater. Chem. Front.* **2019**, *3*, 1062.

[55] K. Zhao, H. Hu, E. Spada, L. K. Jagadamma, B. Yan, M. Abdelsamie, Y. Yang, L. Yu, R. Munir, R. Li, G. O. N. Ndjawa, A. Amassian, *J. Mater. Chem. A* **2016**, *4*, 16036.

[56] J. H. Kim, A. Gadisa, C. Schaefer, H. Yao, B. R. Gautam, N. Balar, M. Ghasemi, I. Constantinou, F. So, B. T. O'Connor, K. Gundogdu, J. Hou, H. Ade, *J. Mater. Chem. A* **2017**, *5*, 13176.

[57] J. J. Van Franeker, M. Turbiez, W. Li, M. M. Wienk, R. A. J. Janssen, *Nat. Commun.* **2015**, *6*, 6229.

[58] C. Schaefer, P. Van Der Schoot, J. J. Michels, *Phys. Rev. E* **2015**, *91*, 022602.

[59] L. Ye, S. Li, X. Liu, S. Zhang, M. Ghasemi, Y. Xiong, J. Hou, H. Ade, *Joule* **2019**, *3*, 443.

[60] L. Ye, B. A. Collins, X. Jiao, J. Zhao, H. Yan, H. Ade, *Adv. Energy Mater.* **2018**, *8*, 1703058.

[61] M. Myahkostupov, F. N. Castellano, *Tetrahedron* **2015**, *71*, 9519.

[62] A. Hexemer, W. Bras, J. Glossinger, E. Schaible, E. Gann, R. Kirian, A. MacDowell, M. Church, B. Rude, H. Padmore, *J. Phys.: Conf. Ser.* **2010**, *247*, 012007.

[63] E. Gann, A. T. Young, B. A. Collins, H. Yan, J. Nasiatka, H. A. Padmore, H. Ade, A. Hexemer, C. Wang, *Rev. Sci. Instrum.* **2012**, *83*, 045110.